

Tunable proximity effects and topological superconductivity in ferromagnetic hybrid nanowiresSamuel D. Escribano¹, Elsa Prada², Yuval Oreg³, and Alfredo Levy Yeyati^{1,*}¹*Departamento de Física Teórica de la Materia Condensada C5, Condensed Matter Physics Center (IFIMAC) and Instituto Nicolás Cabrera, Universidad Autónoma de Madrid, E-28049 Madrid, Spain*²*Instituto de Ciencia de Materiales de Madrid (ICMM), Consejo Superior de Investigaciones Científicas (CSIC), E-28049 Madrid, Spain*³*Department of Condensed Matter Physics, Weizmann Institute of Science, Rehovot 7610, Israel*

(Received 13 November 2020; accepted 1 July 2021; published 19 July 2021)

Hybrid semiconducting nanowire devices combining epitaxial superconductor and ferromagnetic insulator layers have been recently explored experimentally as an alternative platform for topological superconductivity at zero applied magnetic field. In this proof-of-principle work we show that the topological regime can be reached in actual devices depending on some geometrical constraints. To this end, we perform numerical simulations of InAs wires in which we explicitly include the superconducting Al and magnetic EuS shells, as well as the interaction with the electrostatic environment at a self-consistent mean-field level. Our calculations show that both the magnetic and the superconducting proximity effects on the nanowire can be tuned by nearby gates thanks to their ability to move the wavefunction across the wire section. We find that the topological phase is achieved in significant portions of the phase diagram only in configurations where the Al and EuS layers overlap on some wire facet, due to the rather local direct induced spin polarization and the appearance of an extra indirect exchange field through the superconductor. While of obvious relevance for the explanation of recent experiments, tunable proximity effects are of interest in the broader field of superconducting spintronics.

DOI: [10.1103/PhysRevB.104.L041404](https://doi.org/10.1103/PhysRevB.104.L041404)

Engineering topological superconductivity in hybrid superconductor-semiconductor nanostructures where Majorana zero modes may be generated and manipulated has emerged as a great challenge for condensed matter physics in the last decade [1–3]. While Rashba-coupled proximitized semiconducting nanowires appears as one of the most successful platforms [4,5], reaching the topological regime in these devices requires applying large magnetic fields. This turns out to be not only detrimental to superconductivity, but it also imposes some constraints in the design of quantum information processing devices [6,7].

Recent experiments [8–10] have been exploring an alternative route in which an epitaxial layer of a ferromagnetic insulator is also added to the superconductor-semiconductor nanowire system. While the idea of replacing the external magnetic field by the ferromagnetic layer appears as rather straightforward in simplified models [11], there are open questions when applied to realistic systems. Microscopic calculations are required to demonstrate whether or not the topological regime could be reached for the actual geometrical and material parameters, as well as gating conditions. Moreover, understanding the interplay of magnetic and superconducting proximity effects in such devices is of relevance in the broader field of superconducting spintronics [12,13] and quantum thermodevices [14,15].

To address this problem we perform comprehensive numerical simulations of the ferromagnetic hybrid nanowire devices (see Fig. 1). Related studies have been performed

concurrently [16–19]. We include the interaction with the electrostatic environment that typically surrounds the hybrid nanostructures by solving the Schrödinger-Poisson equations self-consistently in the Thomas-Fermi approximation.

We show that topological superconductivity can indeed arise in these systems provided that certain geometrical and electrostatic conditions are met. We find that, for realistic values of the external gates, device layouts where the Al and EuS layers that partially cover the wire overlap on one facet develop extended topological regions in parameter space with significant topological gaps. This is in contrast to devices where the superconducting and magnetic layers are grown on adjacent facets. This could explain why recent experiments find zero-bias peaks in bias spectroscopy experiments—compatible in principle with the existence of a Majorana zero mode at the wire’s end—only in the former geometry but not in the latter.

Concerning the magnetization process, an open issue is whether the spin polarization is directly induced by the ferromagnet in the semiconducting nanowire electrons, or indirectly through a more elaborate process where it is first induced in the superconducting layer (at the regions where the Al and EuS shells overlap) and then in the wire. For instance, Ref. [8] suggested that the hysteretic behavior found in some devices could be in agreement with the indirect mechanism. We find that there is indeed an indirect induced magnetization through the Al layer, but this cannot drive a topological phase transition by itself. Conversely, there is strong direct magnetization from the EuS into the InAs, but only over a very thin region close to the ferromagnet. Interestingly, both mechanisms—direct and indirect—contribute to

*Corresponding author: a.l.yeyati@uam.es

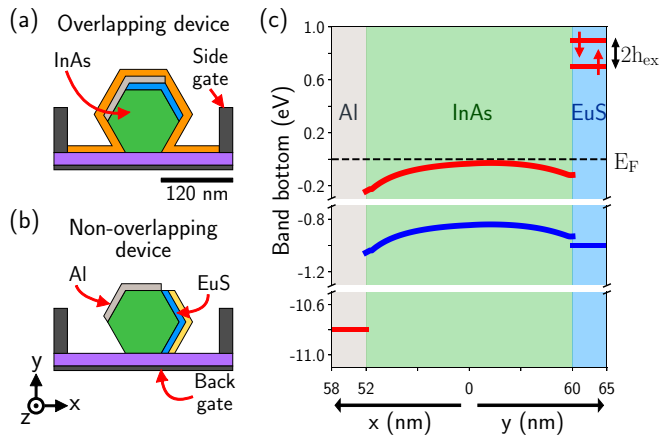


FIG. 1. Hybrid nanowire geometries. (a, b) Sketches of the devices studied in this work: a hexagonal cross-section InAs nanowire (green) is simultaneously proximitized by an Al superconductor layer (light grey) and an EuS magnetic insulator layer (blue). Two side gates and one back gate (dark grey) allow to tune the chemical potential and control the position of the wavefunction inside the heterostructure. Different dielectrics are used in the experiments [8] to allow gating (SiO_2 , in purple) and to avoid the oxidation of the EuS layer (HfO_2 and AlO_2 , in orange and yellow, respectively). In the overlapping device, (a), the Al and EuS layers overlap on one facet, while in the nonoverlapping device, (b), they are grown on different facets. (c) Diagram of the conduction- and valence-band edge positions (in red and blue, respectively) across the heterostructure, spanning the three different materials. In the Al and InAs, the Fermi energy is located in the conduction band (close to the band bottom in InAs), whereas in the EuS it is inside its insulating gap. The EuS conduction band is spin splitted (being h_{ex} the exchange coupling). For this simulation we fix all gate voltages to zero.

achieve robust and sizable topological regions in the phase diagram.

Finally, as a guide for future experiments, we elucidate the role of external potential gates in current device layouts. We show that the topological phase depends critically on the nanowire wavefunction location, a property that can be controlled by tuning appropriately those gates.

Device geometries and model. Following closely the experiments of Ref. [8], we consider the two types of device geometries depicted in Figs. 1(a) and 1(b). In both cases, a hexagonal cross-section InAs nanowire is partially covered by epitaxial Al and EuS layers. The main difference between them is that, in the overlapping device [Fig. 1(a)], the Al and EuS layers partially overlap on one facet, while in the nonoverlapping one [Fig. 1(b)], they lie on adjacent facets. Various dielectrics surrounding the hybrid wires are included in our electrostatic simulations although we find that they play a minor role. Last, there are three gate electrodes used in the experiments to tune the electrostatic potential inside the devices: one back gate and two side gates. We analyze other geometries in the Supplemental Material (SM) [20].

In this work we address the bulk electronic properties of these hybrid nanowires, which we assume are translational invariant along the z direction. A schematic band diagram of the three different materials in the transverse directions, x, y , can be seen in Fig. 1(c). The Al layer is a metal whose conduction

band lies at -11.7 eV below the Fermi level [21]. Despite the fact that the conduction band of the InAs is typically at the Fermi level, experimental angle-resolved photoemission spectroscopy (ARPES) [22] and scanning tunneling microscopy (STM) [23] measurements on epitaxial Al/InAs structures show that there is a band offset of ~ 0.2 eV between the Al and the InAs. This imposes an electron doping of the InAs conduction band close to the Al/InAs interface. On the other hand, soft x-ray ARPES (SX-ARPES) experiments on the EuS/InAs interface [9] indicate that the InAs conduction band lies well within the EuS band gap, which is of the order of 1.7 eV [24]. In particular, the EuS conduction band is located 0.7 eV above the Fermi level and the $4f$ valence bands 1 eV below [9,24]. The EuS conduction band is characterized by an exchange field h_{ex} that shifts the spin-up and spin-down energies by roughly ± 100 meV [25–27]. In addition to this, and similarly to the InAs/Al interface, SX-ARPES experiments [9] also revealed a band bending of the order of 0.1 eV at the InAs/EuS interface, which imposes a smaller charge accumulation at this junction as well. All these band alignments are further distorted by the electric fields defined by the gate electrodes. However, for sufficiently small fields one can assume that only the InAs conduction band moves and can neglect its hybridization with the EuS valence bands (see the SM [20] for further details).

Under these assumptions, we describe the wires using the following continuous model Hamiltonian:

$$H = \left[\vec{k}^T \frac{\hbar^2}{2m_{\text{eff}}(\vec{r})} \vec{k} - E_F(\vec{r}) + e\phi(\vec{r}) + h_{\text{ex}}(\vec{r})\sigma_z \right] \tau_z + \frac{1}{2} [\vec{\alpha}(\vec{r}) \cdot (\vec{\sigma} \times \vec{k}) + (\vec{\sigma} \times \vec{k}) \cdot \vec{\alpha}(\vec{r})] \tau_z + \Delta(\vec{r})\sigma_y \tau_y, \quad (1)$$

where $\vec{r} = (x, y)$, $\vec{k} = (-i\vec{\nabla}_r, k_z)$, and σ_α and τ_α denote Pauli matrices in spin and Nambu spaces, respectively. The parameters m_{eff} , E_F , h_{ex} , and Δ , corresponding to the effective mass, Fermi energy, exchange field, and superconducting pairing amplitude, are taken differently for each region according to estimations from the literature, as summarized in Table I of the SM [20]. To simulate the disordered outer surface of the Al layer and the irregular EuS/Al interface we introduce a random Gaussian noise in $E_F(\vec{r})$ [20]. The other parameters, i.e., the electrostatic potential $\phi(\vec{r})$ and the spin-orbit coupling (SOC) inside the wire $\alpha(\vec{r})$, are determined in a self-consistent way. For this purpose, we obtain $\phi(\vec{r})$ by solving the Schrödinger-Poisson equations within the Thomas-Fermi approximation [28,29]. The SOC $\alpha(\vec{r})$ varies locally with the electric field and is accurately calculated using the procedure described in Ref. [30] (see also [20]). Notice that the exchange field does not give rise to a magnetic orbital term in the Hamiltonian, as opposed to what happens in wires under an external magnetic field [31–34].

To obtain the electronic properties we diagonalize Eq. (1). To this end, we discretize it into a tight-binding Hamiltonian using an appropriate mesh, which is dictated by the Al Fermi wavelength [20]. Notice that a description of the three material regions (Al, InAs, and EuS) on the same footing constitutes a demanding computational task. In the second part of this work we build a simplified model in which we integrate out the Al and EuS layers and include their proximity effects over the

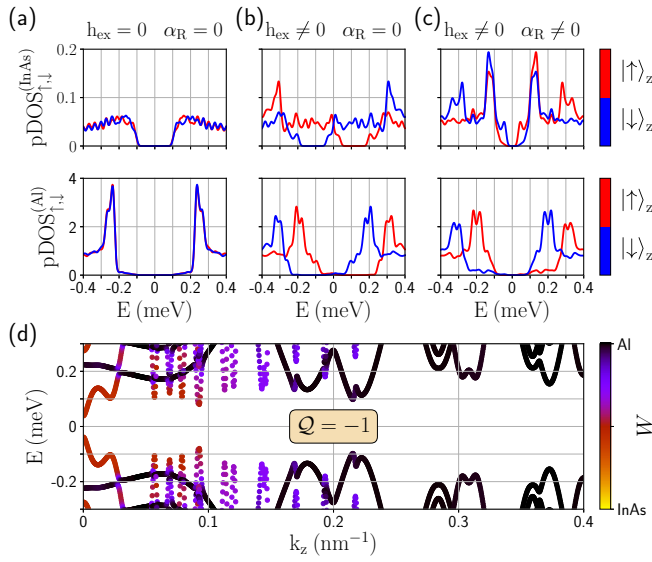


FIG. 2. Full model results. (a–c) Spin-resolved partial density of states (pDOS) for the overlapping device integrated over the InAs wire volume (top row) and the Al layer volume (bottom row) when (a) the exchange field h_{ex} in the EuS layer and the Rashba SOC α_{R} in the InAs wire are set to zero, (b) only the exchange field is turned on, and (c) both are present. Red and blue correspond to the pDOS for different spin orientations along the z axis (wire’s direction). (d) Low-energy band structure versus k_z for the hybrid-wire parameters in (c). The color bar represents the relative weight W of a given state in the Al layer (black) and in the InAs wire (yellow). The wavefunction weight in the EuS layer is negligible since it is an insulating material. The \mathbb{Z}_2 topological invariant is $\mathcal{Q} = -1$, signaling a topological phase. We take here $V_{\text{bg}} = -0.95$ V and $V_{\text{sg}}^{(\text{L,R})} = 0$ V. Other parameters can be found in Table I of the SM.

InAs wire as position-dependent effective parameters. This allows us to explore the system’s phase diagram for a broader range of parameters.

Full model results. We first focus on the density of states (DOS) and dispersion relation of the overlapping geometry (see Fig. 2) fixing the side-gate voltages to zero and the back gate to ~ -1 V. In order to identify the separate effect of the magnetic and superconducting terms, we perform three different calculations: in the first one we switch off the exchange field in the EuS and the Rashba SOC in the InAs [Fig. 2(a)]; then we switch on h_{ex} [Fig. 2(b)] and finally we also connect α_{R} [Fig. 2(c)].

In the top panel of Fig. 2(a) we show the partial DOS integrated over the InAs volume. It exhibits a well-defined induced superconducting gap, although halved with respect to the ~ 0.2 meV gap observed in the DOS integrated over the Al shell volume [Fig. 2(a), bottom panel]. This is in accordance with what one expects from a conventional superconducting proximity effect [34–36].

When $h_{\text{ex}} \neq 0$ (but $\alpha_{\text{R}} = 0$) we observe two main features in the spin-resolved partial DOS. First, an energy splitting of the superconducting coherence peak appears in the Al [Fig. 2(b), bottom panel], which is of the order of ~ 0.06 meV, in agreement with recent theoretical and experimental results on Al/EuS junctions [37–40]. This agreement without any

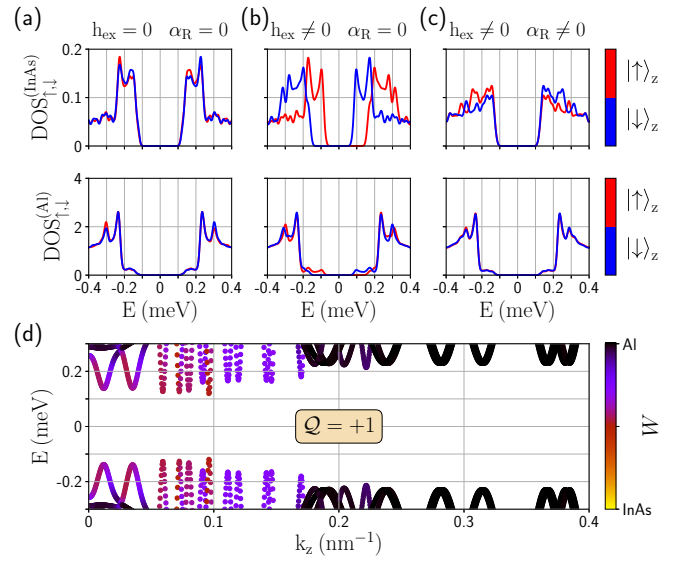


FIG. 3. Same as in Fig. 2 but for the nonoverlapping device. The \mathbb{Z}_2 topological invariant in (d) is now $\mathcal{Q} = 1$, signaling a trivial phase.

fine tuning of the parameters in our model is encouraging about its validity. Second, there is a complete closing of the induced gap in the InAs [Fig. 2(b), top panel]. This points to an induced exchange field larger than ~ 0.1 meV, the induced gap in the semiconductor, and therefore, larger than in the Al layer. In contrast to previous proposals [8,10] our results suggest that in the current case topological superconductivity is achieved below the Chandrasekar-Clogston limit [41,42] for the Al ($h_{\text{ex}}^{(\text{Al})} < \Delta/\sqrt{2}$).

Finally, in Fig. 2(c) (top panel) we observe that a gap is opened again in the presence of SOC. This sequence of gap closing and reopening at a high-symmetry k_z point is a signature of a topological phase transition. The band structure shown in Fig. 2(d) further illustrates the spatial distribution of the low-energy states in this last case (i.e., with $h_{\text{ex}} \neq 0$ and $\alpha_{\text{R}} \neq 0$). The weight W of each state in the different materials is represented with colors, from a state completely located in the Al layer (black) to one completely located in the InAs wire (yellow). The lowest-energy states close to $k_z = 0$ have significant weight both in the Al and in the InAs, as expected for a topological superconducting phase [34]. We prove that the system in Figs. 2(c) and 2(d) is indeed in the topological regime by calculating the \mathbb{Z}_2 topological invariant \mathcal{Q} . For large Hamiltonian matrices, this can be achieved by computing the Chern number from the eigenvalues of the Wilson matrix, which only involves the lowest-energy eigenstates at the Brillouin zone borders [20]. We find $\mathcal{Q} = -1$, which actually corresponds to the nontrivial case.

Strikingly, the same analysis for the nonoverlapping geometry (Fig. 3) reveals that the magnetic proximity effect in this case is not strong enough to close and reopen the superconducting gap in the wire. The reason for this behavior can be traced to the limited spin polarization induced in the nanowire for this geometry. Hence, there is no topological phase in this case, at least for this choice of gate voltages.

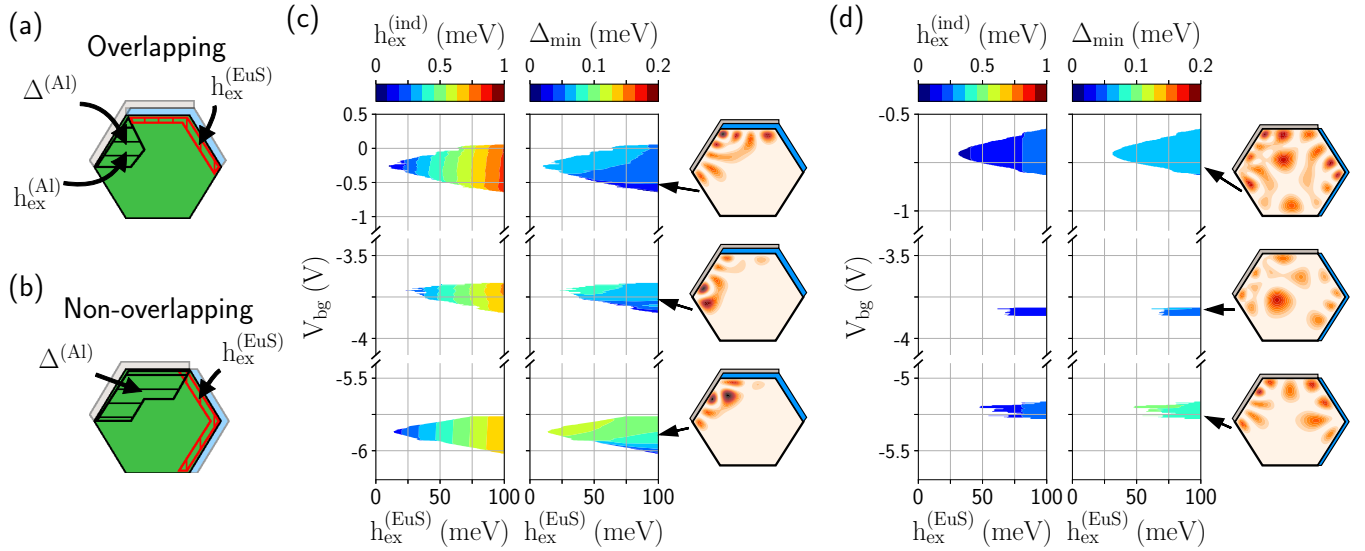


FIG. 4. Simplified-model results. The Al and EuS layers are integrated out and their respective effective induced pairing amplitude and exchange field on the InAs wire are included within the streaked regions shown in the sketches of (a) the overlapping device and (b) the nonoverlapping one. We take $\Delta^{(\text{Al})} = 0.23$ meV and $h_{\text{ex}}^{(\text{Al})} = 0.06$ meV over a wide region of 45 nm near the Al interface. $h_{\text{ex}}^{(\text{Al})}$ is only present in (a) where the Al and the EuS are in contact. We include $h_{\text{ex}}^{(\text{EuS})}$ over a thin region of 1 nm close to the EuS layer. (c) Topological phase diagram of the overlapping device versus back-gate potential, V_{bg} , and exchange field at the EuS-InAs interface, $h_{\text{ex}}^{(\text{EuS})}$, for $V_{\text{sg}}^{(\text{L,R})} = 0$. In the topological regions, we show with colors the expectation value of the induced exchange field (left panel), the topological minigap (middle panel), and the wavefunction profile (right panel), all of them for the transverse subband closest to the Fermi energy. The parameters for which the wavefunctions are plotted are indicated with arrows. (d) Same as (c) but for the nonoverlapping device and fixing $V_{\text{sg}}^{(\text{R})} = 2$ V and $V_{\text{sg}}^{(\text{L})} = 0$. The values of $V_{\text{sg}}^{(\text{L,R})}$ in (c) and (d) are taken to maximize the topological regions in each case. Other parameters can be found in Table I of the SM [20]. The extension of the topological phase is very much reduced with respect to (c) (almost negligible for some subbands) both in the V_{bg} and $h_{\text{ex}}^{(\text{EuS})}$ axes. Moreover, in the regions where it is present, the topological gap is small. In contrast, large topological regions with stronger minigaps are found for the overlapping device. The reason is twofold: (i) the wavefunction can be pushed simultaneously close to the Al and EuS layers due to the electrostatics of the overlapped shells, which increases the superconducting and magnetic proximity effects; (ii) the induced exchange field feeds both from the direct and indirect contributions in this case.

Simplified model and phase diagram. We consider now the Hamiltonian of Eq. (1) restricted to the InAs wire, where we include an effective pairing amplitude $\Delta^{(\text{Al})} = 0.23$ meV and an exchange field $h_{\text{ex}}^{(\text{EuS})} = 100$ meV on the cross-section regions closer to the Al and the EuS shells, respectively, as schematically depicted in Figs. 4(a) and 4(b). We also include a smaller exchange coupling $h_{\text{ex}}^{(\text{Al})} = 0.06$ meV in the Al-proximitized region of the overlapping device. The magnitude of these parameters and the extension of the corresponding regions are extracted by adjusting to the behavior of the full model results, as shown in the SM [20].

In Fig. 4(c) we present the topological phase diagram of the overlapping device as a function of the back-gate voltage and the exchange field of the EuS. Notice that $h_{\text{ex}}^{(\text{EuS})}$ should be 100 meV according to our full model. However, departures from the idealized model of Eq. (1) might reduce the value of the induced magnetic exchange. For instance, the mismatch between the minima of the InAs conduction band (at the Γ point) and the EuS one (at the X point [43]) could suppress their hybridization depending on material growth directions or other details (see the SM [20]), leading to a smaller $h_{\text{ex}}^{(\text{EuS})}$ value. Thus we allow this parameter to vary between 0 and 100 meV to evaluate the robustness of our results with respect to this value. With colors, in the left panel of Fig. 4(c) we show the induced exchange coupling, $h_{\text{ex}}^{(\text{ind})} = \langle h_{\text{ex}}(\vec{r})\sigma_z \rangle$ [44], and in the middle panel the induced minigap, $\Delta_{\text{min}} = |E(k_z =$

$k_{\text{F}}]$, for the energy state closest to the Fermi energy in both cases. In these plots, white means trivial (i.e., $\mathcal{Q} = 1$), while the colored regions correspond to the topological phase. There are several topological regions against V_{bg} corresponding to different transverse subbands. In those regions, the condition that $h_{\text{ex}}^{(\text{ind})}$ is larger than the square root of the induced gap squared plus the chemical potential squared is fulfilled, as expected [4,5]. To the right in Fig. 4(c) we show the probability density of the transverse subband closer to the Fermi level at $k_z = 0$ across the wire section for the parameters indicated with arrows. In the three cases exhibited, the wavefunction concentrates both around the left-upper facet covered by Al, and the top facet where the Al and EuS layers overlap. This is consistent with the requirement of maximizing simultaneously the superconducting and magnetic proximity effects.

The phase diagram for the nonoverlapping device is shown in Fig. 4(d). The extension of the topological phase is very much reduced, almost negligible for some subbands. It is interesting to observe that, for realistic gate potential values, the wavefunction needs to be very spread across the wire section in order to acquire the superconducting and magnetic correlations for the topological phase to develop. This in turn translates into narrow back-gate voltage ranges for which this is possible and small topological minigaps.

In the SM [20] we further analyze the previous phase diagrams as a function of the right-side gate voltage, obtaining

similar results. We also consider alternative geometries, nevertheless finding that the overlapping configuration of Fig. 1(a) gives rise to more extended, robust, and tunable topological regions for realistic parameters. In particular, we find that the best way to optimize the topological state (i.e., increase its minigap) is by fixing a large negative back-gate potential and a small positive right-side gate potential. In doing so, the wavefunction is pushed towards the superconductor-ferromagnet corner of the wire and thus the superconducting and magnetic proximity effects are maximized.

Conclusions. From calculations of the DOS, band structure, topological invariant, and the phase diagram, we conclude that the hybrid InAs/Al/EuS nanowires studied in Ref. [8] can exhibit topological superconductivity under certain geometrical and gating conditions. For a topological phase to exist, the nanowire wavefunction must acquire both superconducting and magnetic correlations such that the induced exchange field exceeds the induced pairing. Since the proximity effects occur only in wire cross-section regions close to the Al and EuS layers, the wavefunction needs to be pushed simultaneously close to both materials by means of nearby gates. Our numerical simulations demonstrate that this is electrostatically favorable in device geometries where the Al and EuS shells overlap over some wire facet. This configuration is further advantageous in that, apart from a direct magnetization from the EuS layer in contact to the wire, there is an indirect one through the Al layer, which favors reaching the topological condition. While our model includes the effect of disorder at the Al layer surface and at the EuS/Al interface, we have not considered other sources of disorder, like, e.g., the presence of magnetic domains. However, these

domains can be aligned by the application of a small field that is then switched to zero, as done in Ref. [8]. A subsequent study which considers a fully diffusive Al layer [45] reaches similar conclusions as our work (although disorder increases the induced exchange field required to achieve a topological phase).

Finally, as a side outcome, our microscopic analysis demonstrates the tunability of the magnetic and superconducting induced couplings in the nanowire. This opens up the possibility of engineering the material geometries, their disposition, and the electrostatic environment to enter and abandon the topological regime at will and, thus, the appearance of Majorana modes. These ideas can be applied to other materials and experimental arrangements, which surely will favor more experiments in the field, as well as in other fields such as superconducting spintronics.

Acknowledgments. We would like to thank S. Vaitiekėnas and C. M. Marcus for illuminating discussions on their experimental results. We also thank M. Alvarado and O. Lesser for valuable help with the topological invariant calculation. A.L.Y. and E.P. acknowledge support from the Spanish MICINN through Grants No. FIS2016-80434-P (AEI/FEDER, EU) and No. FIS2017-84860-R, by EU through Grant No. 828948 (AndQC), and through the “María de Maeztu” Programme for Units of Excellence in R&D (Grant No. MDM-2014-0377). Y.O. acknowledges partial support through the ERC under the European Union’s Horizon 2020 research and innovation programme (Grant Agreement LEGOTOP No. 788715), the ISF Quantum Science and Technology (Grant No. 2074/19), the BSF and NSF (Grant No. 2018643), and the CRC/Transregio 183.

-
- [1] R. Aguado, *Riv. Nuovo Cimento* **40**, 523 (2017).
 [2] R. M. Lutchyn, E. P. A. M. Bakkers, L. P. Kouwenhoven, P. Krogstrup, C. M. Marcus, and Y. Oreg, *Nat. Rev. Mater.* **3**, 52 (2018).
 [3] E. Prada, P. San-Jose, M. W. A. de Moor, A. Geresdi, E. J. H. Lee, J. Klinovaja, D. Loss, J. Nygård, R. Aguado, and L. P. Kouwenhoven, *Nat. Rev. Phys.* **2**, 575 (2020).
 [4] R. M. Lutchyn, J. D. Sau, and S. Das Sarma, *Phys. Rev. Lett.* **105**, 077001 (2010).
 [5] Y. Oreg, G. Refael, and F. von Oppen, *Phys. Rev. Lett.* **105**, 177002 (2010).
 [6] S. Plugge, A. Rasmussen, R. Egger, and K. Flensberg, *New J. Phys.* **19**, 012001 (2017).
 [7] T. Karzig, C. Knapp, R. M. Lutchyn, P. Bonderson, M. B. Hastings, C. Nayak, J. Alicea, K. Flensberg, S. Plugge, Y. Oreg, C. M. Marcus, and M. H. Freedman, *Phys. Rev. B* **95**, 235305 (2017).
 [8] S. Vaitiekėnas, Y. Liu, C. M. Marcus, and P. Krogstrup, *Nat. Phys.* **17**, 43 (2021).
 [9] Y. Liu, A. Luchini, S. Martí-Sánchez, C. Koch, S. Schuwalow, S. A. Khan, T. Stankevič, S. Francoual, J. R. L. Mardegan, J. A. Krieger, V. N. Strocov, J. Stahn, C. A. F. Vaz, M. Ramakrishnan, U. Staub, K. Lefmann, G. Aeppli, J. Arbiol, and P. Krogstrup, *ACS Appl. Mater. Interfaces* **12**, 8780 (2020).
 [10] Y. Liu, S. Vaitiekėnas, S. Martí-Sánchez, C. Koch, S. Hart, Z. Cui, T. Kanne, S. A. Khan, R. Tanta, S. Upadhyay, M. E. Cachaza, C. M. Marcus, J. Arbiol, K. A. Moler, and P. Krogstrup, *Nano Lett.* **20**, 456 (2020).
 [11] J. D. Sau, R. M. Lutchyn, S. Tewari, and S. Das Sarma, *Phys. Rev. Lett.* **104**, 040502 (2010).
 [12] S. A. Wolf, D. D. Awschalom, R. A. Buhrman, J. M. Daughton, S. von Molnár, M. L. Roukes, A. Y. Chtchelkanova, and D. M. Treger, *Science* **294**, 1488 (2001).
 [13] J. Linder and J. W. A. Robinson, *Nat. Phys.* **11**, 307 (2015).
 [14] F. Giazotto, T. T. Heikkilä, A. Luukanen, A. M. Savin, and J. P. Pekola, *Rev. Mod. Phys.* **78**, 217 (2006).
 [15] P. Machon, M. Eschrig, and W. Belzig, *Phys. Rev. Lett.* **110**, 047002 (2013).
 [16] B. D. Woods and T. D. Stanescu, *arXiv:2011.01933*.
 [17] A. Maiani, R. Seoane Souto, M. Leijnse, and K. Flensberg, *Phys. Rev. B* **103**, 104508 (2021).
 [18] C.-X. Liu, S. Schuwalow, Y. Liu, K. Vilkelis, A. L. R. Manesco, P. Krogstrup, and M. Wimmer, *arXiv:2011.06567*.
 [19] J. Langbehn, S. Acero González, P. W. Brouwer, and F. von Oppen, *Phys. Rev. B* **103**, 165301 (2021).
 [20] See Supplemental Material at <http://link.aps.org/supplemental/10.1103/PhysRevB.104.L041404> for further details on the parameters and numerical methods used for our simulations, for an additional study of the phase diagram versus the side-gate potential, and for an analysis of a different geometry. The Supplemental Material includes Refs. [46–71].

- [21] N. W. Ashcroft and N. D. Mermin, *Solid State Physics*, Vol. 1 (Saunders College Publishing, Philadelphia, 1976).
- [22] S. Schuwalow, N. B. M. Schroeter, J. Gukelberger, C. Thomas, V. Strocov, J. Gamble, A. Chikina, M. Caputo, J. Krieger, G. C. Gardner, M. Troyer, G. Aeppli, M. J. Manfra, and P. Krogstrup, [arXiv:1910.02735](https://arxiv.org/abs/1910.02735).
- [23] J. Reiner, A. K. Nayak, A. Tulchinsky, A. Steinbok, T. Koren, N. Morali, R. Batabyal, J.-H. Kang, N. Avraham, Y. Oreg, H. Shtrikman, and H. Beidenkopf, *Phys. Rev. X* **10**, 011002 (2020).
- [24] D. E. Eastman, F. Holtzberg, and S. Methfessel, *Phys. Rev. Lett.* **23**, 226 (1969).
- [25] A. Mauger and C. Godart, *Phys. Rep.* **141**, 51 (1986).
- [26] J. S. Moodera, T. S. Santos, and T. Nagahama, *J. Phys.: Condens. Matter* **19**, 165202 (2007).
- [27] B. W. Alphenaar, A. D. Mohite, J. S. Moodera, and T. S. Santos, in *Physical Chemistry of Interfaces and Nanomaterials VIII*, edited by O. L. A. Monti and O. V. Prezhdo (International Society for Optics and Photonics, Bellingham, WA, 2009), Vol. 7396, pp. 24–32.
- [28] A. E. G. Mikkelsen, P. Kotetes, P. Krogstrup, and K. Flensberg, *Phys. Rev. X* **8**, 031040 (2018).
- [29] S. D. Escribano, A. Levy Yeyati, Y. Oreg, and E. Prada, *Phys. Rev. B* **100**, 045301 (2019).
- [30] S. D. Escribano, A. L. Yeyati, and E. Prada, *Phys. Rev. Research* **2**, 033264 (2020).
- [31] B. Nijholt and A. R. Akhmerov, *Phys. Rev. B* **93**, 235434 (2016).
- [32] B. Kiczek and A. Ptok, *J. Phys.: Condens. Matter* **29**, 495301 (2017).
- [33] O. Dmytruk and J. Klinovaja, *Phys. Rev. B* **97**, 155409 (2018).
- [34] G. W. Winkler, A. E. Antipov, B. van Heck, A. A. Soluyanov, L. I. Glazman, M. Wimmer, and R. M. Lutchyn, *Phys. Rev. B* **99**, 245408 (2019).
- [35] W. Chang, S. M. Albrecht, T. S. Jespersen, F. Kuemmeth, P. Krogstrup, J. Nygård, and C. M. Marcus, *Nat. Nanotechnol.* **10**, 232 (2018).
- [36] M. W. A. de Moor, J. D. S. Bommer, D. Xu, G. W. Winkler, A. E. Antipov, A. Bargerbos, G. Wang, N. van Loo, R. L. M. Op het Veld, S. Gazibegovic, D. Car, J. A. Logan, M. Pendharkar, J. S. Lee, E. P. A. M. Bakkers, C. J. Palmstrøm, R. M. Lutchyn, L. P. Kouwenhoven, and H. Zhang, *New J. Phys.* **20**, 103049 (2018).
- [37] X. Hao, J. S. Moodera, and R. Meservey, *Phys. Rev. Lett.* **67**, 1342 (1991).
- [38] E. Strambini, V. N. Golovach, G. De Simoni, J. S. Moodera, F. S. Bergeret, and F. Giazotto, *Phys. Rev. Mater.* **1**, 054402 (2017).
- [39] M. Rouco, S. Chakraborty, F. Aikebaier, V. N. Golovach, E. Strambini, J. S. Moodera, F. Giazotto, T. T. Heikkilä, and F. S. Bergeret, *Phys. Rev. B* **100**, 184501 (2019).
- [40] X. P. Zhang, V. N. Golovach, F. Giazotto, and F. S. Bergeret, *Phys. Rev. B* **101**, 180502(R) (2020).
- [41] B. S. Chandrasekhar, *Appl. Phys. Lett.* **1**, 7 (1962).
- [42] A. M. Clogston, *Phys. Rev. Lett.* **9**, 266 (1962).
- [43] S. Nirpendra, M. Sapan, N. Tashi, and A. Sushil, *Phys. B: Condens. Matter* **388**, 99 (2007).
- [44] Note that the induced exchange coupling in the wire, $h_{\text{ex}}^{(\text{ind})}$, is much smaller (approximately 1% [20]) than the EuS parent Zeeman field, $h_{\text{ex}}^{\text{(EuS)}}$.
- [45] A. Khindanov, J. Alicea, P. Lee, W. S. Cole, and A. E. Antipov, *Phys. Rev. B* **103**, 134506 (2021).
- [46] I. Vurgaftman, J. R. Meyer, and L. R. Ram-Mohan, *J. Appl. Phys.* **89**, 5815 (2001).
- [47] M. Levinshtein, S. Rumyantsev, and M. Shur, *Handbook Series on Semiconductor Parameters*, Vol. 1 (World Scientific, Singapore, 2000).
- [48] C. Thelander, K. A. Dick, M. T. Borgström, L. E. Fröberg, P. Caroff, H. A. Nilsson, and L. Samuelson, *Nanotechnology* **21**, 205703 (2010).
- [49] B. Segall, *Phys. Rev.* **124**, 1797 (1961).
- [50] Y. N. Chiang and M. O. Dzyuba, *Europhys. Lett.* **120**, 17001 (2017).
- [51] R. M. Xavier, *Phys. Lett. A* **25**, 244 (1967).
- [52] J. Axe, *J. Phys. Chem. Solids* **30**, 1403 (1969).
- [53] J. Robertson, *Eur. Phys. J. Appl. Phys.* **28**, 265 (2004).
- [54] S. D. Escribano, Majorana Nanowires Quantum Simulation Package, 2020, <https://zenodo.org/record/3974288#.YPBQ0OgzY2w>.
- [55] A. Altland and M. R. Zirnbauer, *Phys. Rev. B* **55**, 1142 (1997).
- [56] A. P. Schnyder, S. Ryu, A. Furusaki, and A. W. W. Ludwig, *Phys. Rev. B* **78**, 195125 (2008).
- [57] T. A. Loring and M. B. Hastings, *Europhys. Lett.* **92**, 67004 (2010).
- [58] Y.-F. Zhang, Y.-Y. Yang, Y. Ju, L. Sheng, R. Shen, D.-N. Sheng, and D.-Y. Xing, *Chin. Phys. B* **22**, 117312 (2013).
- [59] O. Lesser and Y. Oreg, *Phys. Rev. Research* **2**, 023063 (2020).
- [60] R. Yu, X. L. Qi, A. Bernevig, Z. Fang, and X. Dai, *Phys. Rev. B* **84**, 075119 (2011).
- [61] A. Alexandradinata, Z. Wang, and B. A. Bernevig, *Phys. Rev. X* **6**, 021008 (2016).
- [62] B. Bradlyn, Z. Wang, J. Cano, and B. A. Bernevig, *Phys. Rev. B* **99**, 045140 (2019).
- [63] A. E. Antipov, A. Bargerbos, G. W. Winkler, B. Bauer, E. Rossi, and R. M. Lutchyn, *Phys. Rev. X* **8**, 031041 (2018).
- [64] S. D. Escribano, A. L. Yeyati, and E. Prada, *Beilstein J. Nanotechnol.* **9**, 2171 (2018).
- [65] B. D. Woods, S. Das Sarma, and T. D. Stanescu, *Phys. Rev. B* **101**, 045405 (2020).
- [66] A. Logg and G. N. Wells, *ACM Trans. Math. Software* **37**, 1 (2010).
- [67] A. Logg, K.-A. Mardal, G. N. Wells *et al.*, *Automated Solution of Differential Equations by the Finite Element Method* (Springer, Berlin, 2012).
- [68] T. Campos, P. E. Faria Junior, M. Gmitra, G. M. Sipahi, and J. Fabian, *Phys. Rev. B* **97**, 245402 (2018).
- [69] R. Winkler, S. Papadakis, E. De Poortere, and M. Shayegan, *Spin-Orbit Coupling in Two-Dimensional Electron and Hole Systems*, Vol. 41 (Springer, Berlin, 2003).
- [70] M. Gmitra and J. Fabian, *Phys. Rev. B* **94**, 165202 (2016).
- [71] P. E. Faria Junior, T. Campos, C. M. O. Bastos, M. Gmitra, J. Fabian, and G. M. Sipahi, *Phys. Rev. B* **93**, 235204 (2016).